國　立　交　通　大　學

機 械 工 程 學 系

碩 士 論 文

垂直圓柱容器中一空氣圓形噴流衝擊至一加熱圓盤之不穩定渦流特性

Characteristics of Unstable Vortex Flow Resulting from a Round Jet of Air Impinging onto a Heated Horizontal Disk Confined in a Vertical Cylindrical Chamber

研　究　生: 吳 佳 鴻

指 導 老 師: 林 清 發 博 士

中 華 民 國 九十三 年 六 月

垂直圓柱容器中一空氣圓形噴流衝擊至一加熱圓盤之不穩定渦流特性

Characteristics of Unstable Vortex Flow Resulting from a Round Jet of Air Impinging onto a Heated Horizontal Disk Confined in a Vertical Cylindrical Chamber

研 究 生：吳 佳 鴻

指導教授：林 清 發

Student：Jia-Hong Wu

Advisor：Tsing-Fa Lin

國立交通大學

機械工程學系

碩士論文

Submitted to Institute of Mechanical Engineering

Collage of Engineering

National Chiao Tung University

In Partial Fulfillment of the Requirements

For the degree of

Master of Science

In

Mechanical Engineering

June 2004

Hsinchu, Taiwan, Republic of China

中 華 民 國 九 十 三 年 六 月

誌 謝

時光飛逝，轉眼間兩年的研究所匆匆過去，在此獲得更深一層的學問且生活上的歷練更加成熟。本論文得以順利完成，首先要感謝指導老師 林清發教授嚴謹及殷切的教導，使學生培養出獨立思考、釐清並解決問題的能力。並特別感謝博士班謝瑞青學長在這兩年期間在實驗、求學以及生活上都給予最大的啟示，亦感謝博士班學長郭威伸、賴佑民、陳尚緯、謝汎鈞等學長在課業上指導及生活中的樂趣都帶給我不同的感受。

還有我同窗好友：小蘇、小白及介哥，兩年來一起渡過了生活及課業上的種種辛酸和欣喜，之間的情誼無與言語。還有也謝謝學弟們，阿賢，小柯，小銘和小劉的熱心幫忙。更要感謝我高中的老師蔡媛琪老師，給予我很大的支持，提供了我許許多多的生活經驗，只有一句話對妳說：「認識妳真好」。還有我高中的朋友們，假期的歡樂亦是由你們陪我渡過，舒緩壓力，快十年的感情到現在依舊沒變，往後也希望跟你們一起渡過。

最後更要感謝我的爺爺默默的保佑我，還有陪我二十幾年的父母，感謝你們讓我有這麼多空間獨立思考，給予我最大的支持與付出；謝謝大姐靜美、二姐雅琪和弟弟俊緯，在這段期間常常麻煩你們幫我解決問題，不厭其煩的陪伴我，真的很感謝我的家人，與你們相處是我這輩子最大的幸福。最後特別要感謝陪我一年多的朋友慧真，雖然認識妳一年多，但似乎已經認識很久的老朋友，碩士的生活最精采的部分是妳陪我渡過，不管在課業上或生活上互相討論、了解和關心，這段歲月裡感謝妳陪我渡過與支持－「有妳真好」。

僅以本文獻給我所關心的人和所有關心我的人。

佳鴻 謹致

2004/06/30 于風城交大

垂直圓柱容器中一空氣圓形噴流衝擊至

一加熱圓盤之不穩定渦流特性

研究生：吳 佳 鴻　　　指導老師： 林 清 發 博士

國立交通大學機械工程學系

中 文 摘 要

本篇論文利用實驗流場觀測方法及溫度場量測方法對於垂直圓柱容器中一高速空氣圓形噴流衝擊至一加熱圓盤之可能產生新的慣性力驅動渦流和一些獨特的週期性混合對流渦流流場特性進行研究。在本實驗研究中，我們藉由拍攝流場結構的上視圖以及側視圖以釐清這些新的渦流特性。實驗的操作範圍分別是：噴流出口到加熱底板間的距離變化 10.0～30.0 mm，流量變化 0～12.0 slpm，相對於雷諾數變化 0～1,623，加熱圓盤與入口冷空氣間的溫度差範圍 0～25.0℃，相對於雷利數 0～63,420。

在本篇論文的實驗結果顯示了在實驗爐體中足夠高的雷諾數下，會產生慣性力驅動的三次和四次渦流。在更高的雷諾數，由於慣性力的驅動致使這渦流流場變成不穩定。在較大的浮慣比會形成浮力所驅動的不穩定，增加雷諾數則變成穩定，在較小的浮慣比下會形成慣性力所驅動的不穩定，此過程只發生在噴流出口到加熱底板間的距離為 20.0 mm 情況下。在高的噴流出口到加熱底板間的距離 30.0 mm，由於慣性力及浮力所驅動渦流相當的大且相連在一起，所以整各流場不穩定的運動狀態則是由兩者互相推擠所造成。特別注意在噴流出口到加熱底板間的距離為 10.0 & 20.0 mm 慣性力所驅動的三次及四次渦流的臨界雷諾數隨著加熱圓盤與入口冷空氣間的溫度差的增加而增加，但是在噴流出口到加熱底板間

的距離為 30.0 mm 則相反，並指出會隨著加熱圓盤與入口冷空氣間的溫度差的增加使渦流流場更容易產生不穩定。

Characteristics of Unstable Vortex Flow Resulting from a Round Jet of Air Impinging onto a Heated Horizontal Disk Confined in a Vertical Cylindrical Chamber

Student: Jia-Hong Wu **Advisor: Prof. Tsing-Fa Lin**

Institute of Mechanical Engineering

National Chiao Tung University

ABSTRACT

An experiment combining flow visualization and temperature measurement is carried out in the present study to investigate the possible presence of new inertia-driven vortex rolls and some unique characteristics of the time-dependent mixed convective vortex flow resulting from a high speed round air jet impinging onto a heated horizontal circular disk in a vertical cylindrical chamber. The flow photos taken from the side and top views of the vortex flow in the chamber aim to unravel these new vortex flow characteristics. In the present experiment the jet-to-disk separation distance is varied from 10.0 to 30.0 mm and the jet flow rate is varied from 0 to 12.0 slpm (standard liter per minute) for the jet Reynolds number Re_j ranging from 0 to 1,623. The temperature difference between the disk and the air injected into the chamber is varied from 0 to 25.0℃ for the Rayleigh number Ra ranging from 0 to 63,420.

The results from the flow visualization clearly show that at sufficiently high Re_j the inertia-driven tertiary and quaternary rolls can be induced. At even slightly higher Re_j the vortex flow becomes unstable due to the inertia-driven flow instability.

Only for H=20.0 mm the flow is subjected to the buoyancy-driven instability. Because of the simultaneous presence of the inertia- and buoyancy-driven instabilities, a reverse flow transition can take place in the chamber with H=20.0 mm. At the large H of 30.0 mm the flow unsteadiness results from the mutual pushing and squeezing of the inertia- and buoyancy-driven rolls since they are relatively large and contact with each other. It is also noted that the critical jet Reynolds number for the onset of tertiary and quaternary rolls increase with ΔT for H=10.0 & 20.0 mm. But for H=30.0 mm the opposite is true, indicating that raising ΔT can destabilize the vortex flow.

TABLE OF CONTENTS

ABSTRACT		**i**
TABLE OF CONTENTS		**iii**
LIST OF TABLES		**v**
LIST OF FIGURES		**vi**
NOMENCLATURE		**xv**
CHAPTER 1	**INTRODUCTION**	**1**
	1.1 Motivation	**1**
	1.2 Literature Review	**2**
	1.3 Objective and Scope of Present Study	**6**
CHAPTER 2	**EXPERIMENTAL APPARATUS AND PROCEDURES**	**9**
	2.1 Experimental Apparatus	**9**
	2.2 Experimental Procedures	**12**
CHAPTER 3	**DIMENSIONLESS GROUPS AND UNCERTAINTY ANALYSIS**	**16**
	3.1 Dimensionless Groups	**16**
	3.2 Uncertainty Analysis	**16**
CHAPTER 4	**RESULTS AND DISCUSSION**	**20**
	4.1 New Steady Vortex Flow Pattern	**21**
	4.2 Onset of Vortex Rolls	**23**
	4.3 Instability of Vortex Flow	**25**
	4.4 Inertia-Driven Time-Dependent Vortex Flow	**27**
	4.5 Characteristics of Buoyancy-Driven Time-Dependent	**31**

Flow

4.6 Flow Regime Maps **33**

CHAPTER 5 Concluding Remarks **105**

REFERECES **107**

LIST OF TABLES

Table 3.1 Summary of uncertainty analysis.

Table 4.1 Critical condition for appearance of the tertiary and quaternary inertia-driven rolls.

Table 4.2 Critical condition for onset of the inertia-driven time periodic flow for various H.

Table 4.3 Critical condition for onset of the inertia-driven nonperiodic flow for various H.

LIST OF FIGURES

Fig. 1.1 Schematic of the flow patterns in a confined impinging jet depicting the plug-flow, buoyancy-induced flow and rotation-induced flow.

Fig. 1.2 Flow regimes associated with a circular jet impinging onto a flat plate.

Fig. 2.1 Schematic diagram of the experimental apparatus.

Fig. 2.2 The heater consists of three parts: resistance heating element, holder and insulator.

Fig. 2.3 The locations of the detection points on the upper copper plate.

Fig. 4.1 Steady side view flow pattern in the chamber with H=30.0 mm for Re_j=270 (Q_j=2.0 slpm) and Ra=63,420 ($\Delta T = 25.0$ ℃): (a)top view flow photo taken at middle horizontal plane halfway between the pipe exit and heated disk, (b) side view flow photo taken at the vertical plane $\theta = 0^\circ$ & $\theta = 180^\circ$ and (c) the corresponding schematically sketched cross plane vortex flow.

Fig. 4.2 Steady vortex flow pattern in the chamber with H=20.0 mm for Re_j=784 (Q_j=5.8 slpm) and Ra=3,760 ($\Delta T = 5.0$ ℃): (a) side view flow photo taken at the vertical plane $\theta = 0^\circ$ and (b) the corresponding schematically sketched cross plane vortex flow.

Fig. 4.3 Steady vortex flow pattern in the chamber with H=10.0 mm for Re_j=1,150 (Q_j=8.5 slpm) and Ra=470 ($\Delta T = 5.0$ ℃): (a) side view flow photo taken at the vertical plane $\theta = 0^\circ$ and (b) the corresponding schematically sketched cross plane vortex flow.

Fig. 4.4 Steady side view flow photos taken at the cross plane $\theta = 0°$ for various Reynolds numbers at H=20.0 mm for Ra= (a) 3,760 (△T=5.0℃) and (b) 7,520 (△T=10.0℃).

Fig. 4.5 Steady side view flow photos taken at the cross plane $\theta = 0°$ for various jet Reynolds numbers at H=10.0 mm for Ra= (a) 470

(△T=5.0°C) and (b) 2,350 (△T=25.0°C).

Fig. 4.6 Steady side view flow photos taken at the cross plane θ=0° for various Rayleigh numbers at Re_j=771 (Q_j=5.7 slpm) and H=20.0 mm.

Fig. 4.7 Steady side view flow photos taken at the cross plane θ=0° for various Rayleigh numbers at Re_j=1,150 (Q_j=8.5 slpm) and H=10.0 mm.

Fig. 4.8 Flow region map delineating the number of rolls.

Fig. 4.9 Steady vortex flow patterns in the chamber at Re_j=0 for (a) H=30.0 mm and Ra=63,420 ($\Delta T = 25.0$ °C) and (b) H=45.0 mm and Ra=214,040 ($\Delta T = 25.0$ °C).

Fig. 4.10 Side view flow photos taken at the cross plane $\theta = 0°$ & 180° at certain instants in a time periodic flow for various Rayleigh numbers at Re_j=1,190 (Q_j=8.8 slpm) and H=10.0 mm.

Fig. 4.11 Top view flow photos at certain instants in statistical states taken at middle horizontal plane halfway between the pipe exit and heated disk for various Rayleigh numbers at Re_j=1,190 (Q_j=8.8 slpm) and H=10.0 mm.

Fig. 4.12 Time-periodic vortex flow for H=20.0 mm and Ra=0 ($\Delta T = 0$ °C) at Re_j=839 (Q_j=6.2 slpm) illustrated by (a) side view flow photos taken at the vertical plane $\theta = 0°$ & $\theta = 180°$ at selected time instants in a typical periodic cycle and (b) top view flow photo taken at middle horizontal plane halfway between the pipe exit and heated disk at certain time instant in the cycle (t_p=1.45 sec).

Fig. 4.13 Time-periodic vortex flow for H=20.0 mm and Ra=18,790 ($\Delta T = 25.0$°C) at Re_j=1,028 (Q_j=7.6 slpm) illustrated by (a) side view flow photos taken at the vertical plane $\theta = 0°$ & $\theta = 180°$ at selected time instants in a typical periodic cycle and (b) top view flow photo taken at middle horizontal plane halfway between the pipe exit and heated disk at certain time instant in the cycle (t_p=1.58 sec).

Fig. 4.14 Time-periodic vortex flow for H=30.0 mm and Ra=38,050

($\Delta T = 15.0$°C) at Re_j=676 (Q_j=5.0 slpm) illustrated by (a) side view flow photos taken at the vertical plane $\theta = 0°$ & $\theta = 180°$ at selected time instants in a typical periodic cycle and (b) top view flow photo taken at middle horizontal plane halfway between the pipe exit and heated disk at certain time instant in the cycle (t_p=1.43 sec).

Fig. 4.15 Time-periodic vortex flow for H=30.0 mm and Ra=50,730 ($\Delta T = 20.0$°C) at Re_j=676 (Q_j=5.0 slpm) illustrated by side view flow photos taken at the vertical plane $\theta = 0°$ & $\theta = 180°$ at selected time instants in a typical periodic cycle (t_p=1.43 sec).

Fig. 4.16 Top view flow photos taken at selected time instants in a typical periodic cycle with Ra=50,730 (ΔT=20.0°C), Q=5.0 slpm (Re_j=676) and H=30.0 mm (t_p=1.43 sec).

Fig. 4.17 Time-periodic vortex flow for H=30.0 mm and Ra=63,420 ($\Delta T = 25.0$°C) at Re_j=676 (Q_j=5.0 slpm) illustrated by side view flow photos taken at the vertical plane $\theta = 0°$ & $\theta = 180°$ at selected time instants in a typical periodic cycle (t_p=1.43 sec).

Fig. 4.18 Top view flow photos taken at selected time instants in a typical periodic cycle with Ra=63,420 (ΔT=25.0°C), Q=5.0 slpm(Re_j=676) and H=30.0 mm (t_p=1.43 sec).

Fig. 4.19 Time-periodic vortex flow for H=30.0 mm and Ra=63,420 ($\Delta T = 25.0$°C) at Re_j=541 (Q_j=4.0 slpm) illustrated by side view flow photos taken at the vertical plane $\theta = 0°$ & $\theta = 180°$ at selected time instants in a typical periodic cycle (t_p=1.67 sec).

Fig. 4.20 Top view flow photos taken at selected time instants in a typical periodic cycle with Ra=63,420 (ΔT=25.0°C), Q=4.0 slpm(Re_j=541) and H=30.0 mm (t_p=1.67 sec).

Fig. 4.21 Top view flow photo taken at the middle horizontal plane for Q_j=4.0 slpm (Re_j=541) and ΔT=25.0°C (Ra=63,420) with H=30.0 mm at certain time instant (a) and the corresponding schematically sketched cross plane flow (b) in a typical periodic cycle.

Fig. 4.22 Side view flow photos taken at the cross plane θ=0° for Q_j=4.0 slpm (Re_j=541) and ΔT=25.0℃ (Ra=63,420) with H=30.0 mm at selected time instants (left) and the corresponding schematically sketched cross plane flow (right) in a typical periodic cycle (t_p=1.67 sec).

Fig. 4.23 The time records of non-dimensional air temperature for Ra=63,420 ($\Delta T = 25.0$℃) and Re_j=676 (Q_j=5.0 slpm) with H=30.0 mm at selected locations for (a) Z=0.33, (b) Z=0.50 and (c) Z=0.67 on the cross plane $\theta = 0°$ (t_p=1.43 sec).

Fig. 4.24 The time records of non-dimensional air temperature for Ra=50,730 ($\Delta T = 20.0$℃) and Re_j=676 (Q_j=5.0 slpm) with H=30.0 mm at selected locations on the vertical plane $\theta = 0°$ at Z=0.67 (t_p=1.43 sec).

Fig. 4.25 The time records of non-dimensional air temperature for Ra=38,050 ($\Delta T = 15.0$℃) and Re_j=676 (Q_j=5.0 slpm) with H=30.0 mm at selected locations on the vertical plane $\theta = 0°$ at Z=0.67 (t_p=1.43 sec).

Fig. 4.26 The time records of non-dimensional air temperature and the corresponding power spectrum densities for fixed Re_j for various Rayleigh numbers with H=30.0 mm at location (R, Z) = (0.58, 0.67) on the vertical plane $\theta = 0°$.

Fig. 4.27 The time records of non-dimensional air temperature and the corresponding power spectrum densities for Ra=50,730 and H=30.0 mm at location (R, Z)=(0.58, 0.67) on the vertical plane $\theta = 0°$ for various jet Reynolds numbers Re_j= (a)541, (b)609, (c)676, (d)744 and (e)811.

Fig. 4.28 The time records of non-dimensional air temperature and the corresponding power spectrum densities for Ra=63,420 and H=30.0 mm at location (R, Z)=(0.58, 0.67) on the vertical plane $\theta = 0°$ for various jet Reynolds numbers Re_j= (a)541, (b)609, (c)676, (d)744 and (e)811.

Fig. 4.29 Time-periodic vortex flow for H=30.0 mm and Ra=0 ($\Delta T = 0$℃) at Re_j=879 (Q_j=6.5 slpm) illustrated by side view flow photos taken at the vertical plane $\theta = 0°$ & $\theta = 180°$ at selected time instants in a typical periodic cycle (t_p=1.33 sec).

Fig. 4.30 Time-periodic vortex flow for H=30.0 mm and Ra=12,680 ($\Delta T = 5.0\,^{\circ}C$) at Re_j=879 (Q_j=6.5 slpm) illustrated by side view flow photos taken at the vertical plane $\theta = 0^{\circ}$ & $\theta = 180^{\circ}$ at selected time instants in a typical periodic cycle (t_p=1.23 sec).

Fig. 4.31 Time-periodic vortex flow for H=30.0 mm and Ra=25,370 ($\Delta T = 10.0\,^{\circ}C$) at Re_j=879 (Q_j=6.5 slpm) illustrated by side view flow photos taken at the vertical plane $\theta = 0^{\circ}$ & $\theta = 180^{\circ}$ at selected time instants in a typical periodic cycle (t_p=1.23 sec).

Fig. 4.32 Time-periodic vortex flow for H=30.0 mm and Ra=38,050 ($\Delta T = 15.0\,^{\circ}C$) at Re_j=879 (Q_j=6.5 slpm) illustrated by side view flow photos taken at the vertical plane $\theta = 0^{\circ}$ & $\theta = 180^{\circ}$ at selected time instants in a typical periodic cycle (t_p=1.17 sec).

Fig. 4.33 Time-periodic vortex flow for H=30.0 mm and Ra=50,730 ($\Delta T = 20.0\,^{\circ}C$) at Re_j=879 (Q_j=6.5 slpm) illustrated by side view flow photos taken at the vertical plane $\theta = 0^{\circ}$ & $\theta = 180^{\circ}$ at selected time instants in a typical periodic cycle (t_p=1.11 sec).

Fig. 4.34 Time-periodic vortex flow for H=30.0 mm and Ra=63,420 ($\Delta T = 25.0\,^{\circ}C$) at Re_j=879 (Q_j=6.5 slpm) illustrated by side view flow photos taken at the vertical plane $\theta = 0^{\circ}$ & $\theta = 180^{\circ}$ at selected time instants in a typical periodic cycle (t_p=1.11 sec).

Fig. 4.35 Top view flow photos taken at selected time instants in a typical periodic cycle for Ra=0 (ΔT=0°C), Q=6.5 slpm (Re_j=879) and H=30.0 mm (t_p=1.33 sec).

Fig. 4.36 Top view flow photos taken at selected time instants in a typical periodic cycle for Ra=12,680 (ΔT=5.0°C), Q=6.5 slpm (Re_j=879) and H=30.0 mm (t_p=1.23 sec).

Fig. 4.37 Top view flow photos taken at selected time instants in a typical periodic cycle for Ra=25,370 (ΔT=10.0°C), Q=6.5 slpm (Re_j=879) and H=30.0 mm (t_p=1.23 sec).

Fig. 4.38 Top view flow photos taken at selected time instants in a typical periodic cycle for Ra=38,050 (ΔT=15.0°C), Q=6.5 slpm (Re_j=879) and H=30.0 mm (t_p=1.17 sec).

Fig. 4.39 Tim-periodic top view flow photos taken at selected time instants in a typical periodic cycle for Ra=50,730 (ΔT=20.0°C), Q=6.5 slpm (Re_j=879) and H=30.0 mm (t_p=1.11 sec).

Fig. 4.40 Top view flow photos taken at selected time instants in a typical periodic cycle for Ra=63,420 (ΔT=25.0°C), Q=6.5 slpm (Re_j=879) and H=30.0 mm (t_p=1.11 sec).

Fig. 4.41 Time-periodic vortex flow for H=30.0 mm and Ra=0 ($\Delta T = 0$°C) at Re_j=947 (Q_j=7.0 slpm) illustrated by side view flow photos taken at the vertical plane $\theta = 0°$ & $\theta = 180°$ at selected time instants in a typical periodic cycle (t_p=1.17 sec).

Fig. 4.42 Top view flow photos taken at selected time instants in a typical periodic cycle for Ra=0 (ΔT=0°C), Q=7.0 slpm (Re_j=947) and H=30.0 mm (t_p=1.17 sec).

Fig. 4.43 Side view flow photos taken at the cross plane θ=0° & 180° at steady state or at certain instant in the statistical state for Re_j=879 (Q_j=6.5 slpm) with various Ra at H=20.0mm.

Fig. 4.44 Top view flow photos taken at midheight of the chamber at steady state or at certain instant in the statistical state for Re_j=879 (Q_j=6.5 slpm) and H=20.0 mm for various Ra.

Fig. 4.45 Side view flow photos taken at the cross plane θ=0° & 180° at steady state or at certain instant in the statistical state for Re_j=676 (Q_j=5.0 slpm) with various Ra at H=30.0mm.

Fig. 4.46 Top view flow photos taken at midheight of the chamber at steady state or at certain instant in the statistical state for Re_j=676 (Q_j=5.0 slpm) and H=30.0 mm for various Ra.

Fig. 4.47 Nonperiodic vortex flow for H=30.0 mm and Ra=0 ($\Delta T = 0$°C) at Re_j=1,217 (Q_j=9.0 slpm) illustrated by side view flow photos taken at the vertical plane $\theta = 0°$ & $\theta = 180°$ at selected time instants.

Fig. 4.48 Nonperiodic vortex flow for H=30.0 mm and Ra=38,050 ($\Delta T = 15.0$ ℃) at Re_j=1,217 (Q_j=9.0 slpm) illustrated by side view flow photos taken at the vertical plane $\theta = 0°$ & $\theta = 180°$ at selected time instants.

Fig. 4.49 Nonperiodic vortex flow for H=30.0 mm and Ra=38,050 ($\Delta T = 15.0$ ℃) at Re_j=1,285 (Q_j=9.5 slpm) illustrated by side view flow photos taken at the vertical plane $\theta = 0°$ & $\theta = 180°$ at selected time instants.

Fig. 4.50 Nonperiodic vortex flow for H=30.0 mm and Ra=38,050 ($\Delta T = 15.0$ ℃) at Re_j=1,352 (Q_j=10.0 slpm) illustrated by side view flow photos taken at the vertical plane $\theta = 0°$ & $\theta = 180°$ at selected time instants.

Fig. 4.51 Nonperiodic vortex flow for H=30.0 mm and Ra=38,050 ($\Delta T = 15.0$ ℃) at Re_j=1,420 (Q_j=10.5 slpm) illustrated by side view flow photos taken at the vertical plane $\theta = 0°$ & $\theta = 180°$ at selected time instants.

Fig. 4.52 Nonperiodic vortex flow for H=30.0 mm and Ra=38,050 ($\Delta T = 15.0$ ℃) at Re_j=1,488 (Q_j=11.0 slpm) illustrated by side view flow photos taken at the vertical plane $\theta = 0°$ & $\theta = 180°$ at selected time instants.

Fig. 4.53 Nonperiodic vortex flow for H=30.0 mm and Ra=38,050 ($\Delta T = 15.0$ ℃) at Re_j=1,623 (Q_j=12.0 slpm) illustrated by side view flow photos taken at the vertical plane $\theta = 0°$ & $\theta = 180°$ at selected time instants.

Fig. 4.54 Top view flow photos taken at midheight of the chamber with Ra=38,050 (ΔT=15.0℃) and D_j=10.0 mm at H=30.0 mm for Re_j=(a)1,217, (b)1,285, (c)1,352, (d)1,420, (e)1,488 and (f)1,623.

Fig. 4.55 The time records of non-dimensional air temperature for Ra=38,050 ($\Delta T = 15.0$ ℃) with H=30.0 mm at location (R, Z)=(0.68, 0.67) and $\theta = 0°$ for various Reynolds numbers Re_j= (a)1,217, (b)1,285, (c)1,352, (d)1,420 and (e)1,488.

Fig. 4.56 Side view flow photos at the cross plane θ=0° & 180° at certain time instant in a typical periodic cycle and time records of air temperature at selected locations in the middle horizontal plane Z=0.5 with H=20.0 mm for Re_j=135, Ra=11,270 & D_j=10.0 mm (t_p=21.05 sec).

Fig. 4.57 Time-periodic vortex flow for H=20.0 mm and Ra=11,270 ($\Delta T = 15.0$ ℃) at Re_j=135 (Q_j=1.0 slpm) illustrated by side view flow photos taken at the vertical plane $\theta = 0°$ & 180° at selected time instants in a typical periodic cycle (t_p=21.05 sec).

Fig. 4.58 Nonperiodic vortex flow for H=20.0 mm and Ra=15,030 ($\Delta T = 20.0$ ℃) at Re_j=135 (Q_j=1.0 slpm) illustrated by side view flow photos taken at the vertical plane $\theta = 0°$ & 180° at selected time instants in the statistical state.

Fig. 4.59 The time records of non-dimensional air temperature and the corresponding power spectrum densities for Ra=11,270 ($\Delta T = 15.0$ ℃)at location (R, Z)=(0.52, 0.5) for $\theta = 0°$ with H=20.0 mm for various Reynolds numbers Re_j= (a)81, (b)108, (c)135, (d)189 and (e)230.

Fig. 4.60 The time records of non-dimensional air temperature and the corresponding power spectrum densities for fixed Re_j for various Rayleigh numbers with H=20.0 mm at location (R, Z) = (0.52, 0.5) on the vertical plane $\theta = 0°$.

Fig. 4.61 Flow regime map delineating the temporal state of the vortex flow for H=10.0 mm.

Fig. 4.62 Flow regime map delineating the temporal state of the vortex flow for H=20.0 mm.

Fig. 4.63 Flow regime map delineating the temporal state of the vortex flow for H=30.0 mm.

Fig. 4.64 Side view flow photos taken at the cross plane θ=0° & 180° at steady state or at certain instants in the statistical state for Ra=7,520 (ΔT=10.0℃) for various Re_j at H=20.0mm.

Fig. 4.65 Side view flow photos taken at the cross plane θ=0° & 180° at steady state or at certain instants in the statistical state for Ra=11,270 (ΔT=15.0℃) for various Re_j at H=20.0mm.

Fig. 4.66 Side view flow photos taken at the cross plane θ=0° & 180° at steady state or at certain instants in the statistical state for Ra=25,370 ($\Delta T = 10.0$ ℃) for various Re_j at H=30.0mm.

NOMENCLATURE

D_j	Diameter of jet at the pipe exit (mm)
D_w	Diameter of disk (mm)
f	Main oscillation frequency (Hz)
Gr	Grashof number, $g\beta\Delta TH^3/\nu^2$
g	Gravity vector (m/s^2)
H	Distance between the exit of injection pipe and heated plate (mm)
Nu	Nusselt number
PSD	Power spectrum denstiy
Q_j	Jet flow rate (Standard Liter per Minute, slpm)
r, θ, z	Dimensional coordinate system of cylinder (mm)
R, Θ, Z	Dimensionless coordinate systems of cylinder, $r/R_c, \theta/360^\circ, z/H$
Ra	Rayleigh number, $g\beta\Delta TH^3/\alpha\nu$
Re_j	Reynolds number of injection, $\overline{V}_j D_j/\nu$
T_a	Ambient Temperature (℃)
T_f	Temperature of the heated disk (℃)
T_j	Temperature of injection jet (℃)
T	Time instant (sec)
V_j	Velocity of the air jet at the injection pipe exit (m/s)

Greek symbols

α	Thermal diffusivity (cm^2/s)
β	Thermal expansion coefficient (1/K)
ΔT	Temperature difference between the heated and the air injected (℃)
μ	Coefficient of viscosity (Nm/m^2)
ν	Kinematic viscosity (m^2/s)
Φ	Non-dimensional temperature, $(T-T_j)/(T_f-T_j)$
ρ	Density (kg/m^3)

CHAPTER 1

INTRODUCTION

1.1 Motivation

Over the past several decades the study of a jet impinging onto a flat plate has been mainly motivated by its superior heat transfer capability. The advantage of the highly efficient jet impinging cooling has been applied to many technological processes such as the drying of textiles and paper products, annealing of glass, cooling of gas turbine components and microelectronic equipments, freezing of tissue in cryosurgery, etc. Recently, it was applied to electronics packaging design for the cooling of portable computers by Guarion and Manno [1]. In the microelectronic fabrication industry low speed impinging jets are often employed in the growth of semiconductor thin crystal films on heated silicon wafers through the chemical vapor deposition (CVD) processes and rapid thermal processing (RTP). At low jet speed the buoyancy generated by the heated wafer can be relatively high compared with the jet inertia and the buoyancy driven flow recirculation tends to appear. Meanwhile, at high jet flow rates the jet inertia is prone to induce secondary flow recirculations due to the jet entrainment associated with the viscous shear. In order to obtain high-quality thin films, the flow in the CVD chamber needs to be stable and contains no vortices. Thus the detailed understanding and analysis of the vortex flow characteristics in the low speed impinging jet flow are rather important in the thin crystal film growth.

It has been known for some time that the vortex flow in the CVD chamber is manly affected by the jet inertia, the buoyancy force due to the heated wafer, and the geometry of the chamber. At increasing jet flow rates, the inertia driven vortex flow is no longer small compared to the buoyancy induced vortex flow. The flow in a typical vertical CVD reactor can be classified broadly into three types: (1) plug flow, where the gas flows smoothly over the substrate without any recirculation in the reactor, (2) buoyancy-induced flow, where the buoyancy force associated with the heated substrate induces recirculating flow of the gas, and (3) rotation-induced flow, where a toroidal vortex forms near the reactor wall close to the rotating substrate, as illustrated in Fig. 1.1 according to Biber et al. [2]. In the present study, we intend to unveil some unique characteristics of the vortex flow in a jet impinging vertically downwards onto a horizontal heated plate. These include the possible presence of new vortex rolls, unusual stabilization of the vortex flow at increasing buoyancy, and new types of time periodic vortex flow at certain conditions.

1.2 Literature Review

In what follows the relevant literature on the present study is briefly reviewed. Most of existing studies relevant to the impinging jet deal with heat and mass transfer of a single jet impinging onto a flat plate, emphasizing the high heat transfer efficiency of the jet. According to the flow characteristics of free jets, Mcnaughton and Sinclair [3] identified four main types of jet in their experimental study and classified the jet by its Reynolds number Re_j: (1) dissipated-laminar jet for Re_j<300, (2) fully laminar jet for 300<Re_j<1000, (3) semi-turbulent jet for 1000< Re_j<3000, and (4) fully turbulent jet for Re_j>3000. As illustrated in Fig. 1.2, the flow in a jet impinging vertically onto a plate can be divided into three regions: (1) free jet region: near the nozzle the jet flow mainly moves in the axial direction and is not affected to a noticeable degree by the presence of the impingement surface, (2) stagnation region: which is located between the free jet region and the wall jet region and is characterized by the significant changes in the flow direction, and (3) wall jet region: the dominated velocity component is in the radial direction and the boundary layer over the plate is subject to nearly zero pressure gradient and thickens as it moves radially outwards. Critical review on various aspects of the flow and heat transfer associated with the impinging jets has been conducted by Viskanta [4] and Jambunathan et al. [5]. The impinging jet flow was found to contain a large recirculation vortex around the jet axis and a somewhat smaller adjacent secondary vortex right above the impinging plate in a confined laminar submerged jet (Law and Masliyah [6]). Recently, the recirculating flow resulting from a confined impinging gas jet at low Re_j was visualized by Santen et al. [7 & 8], Cheng et al. [9] and Hsieh et al. [10]. It has been noted that the flow of impinging jet can become unstable as the Rayleigh number exceeds certain critical level. Furthermore, Santen et al. [7 & 8] explained the suppression of the buoyancy induced flow at increasing Reynolds numbers. Hsieh et al. [10] noted that the flow recirculation was in the form of three circular vortex rolls including a primary vortex roll around the jet, a secondary vortex roll in the middle region and a buoyancy-induced vortex roll in the outer zone. The inner and middle vortex rolls are driven by the viscous shear due to a nonuniform velocity distribution in the jet and are stronger and bigger at a high Re_j. Hence they are called the inertia-driven rolls. But the buoyancy driven outer vortex roll is important at high buoyancy-to-inertia ratio. The secondary inertia-driven vortex roll only appears at certain high Re_j and it is much smaller and weaker than the primary inertia-driven vortex roll. Cheng et al. [9] indicated that increasing the chamber pressure and the temperature difference between the heated plate and air jet caused the outer roll to become larger and the inner roll to become correspondingly smaller. Moreover, at high buoyancy and inertia the flow becomes time dependent. Hsieh et al. [10] showed that the vortex flow became time periodic at a certain high buoyancy-to-inertia ratio and the oscillation frequency of the vortex flow increased with Re_j. In a rapid chemical vapor deposition (RCVD) chamber, Rayleigh light scattering method was used to measure temperature and visualize the flow by Horton and Peterson [11]. Their results showed that the flow became unstable at $\mathrm{Gr}/\mathrm{Re}_j^2 = 5$. Recently, heat transfer in confined impinging jets was examined by Hsieh et al. [12]. They concluded that the heat transfer characteristics were only significantly affected by the jet Reynolds number. Moreover, numerical computation using the Reynolds stress model was performed to predict the flow field in confined turbulent jet impingement by Morris et al. [13]. Multiple vortices in the flow were well predicted by the Reynolds stress model (RMS). The k-ε turbulence model was found to be more accurate than the second-moment closure in predicting the turbulent impinging jet flow (Dianat et al. [14]). An experimental study on unconfined impinging jets was conducted to examine flow structure and heat transfer by Carcasci [15] and Angioletti et al. [16]. Their results showed that the convection heat transfer coefficient reached a peak around the stagnation zone for a small nozzle-to-plate distance. More recently, Chung and Luo [17] and Chiriac and Ortega [18] demonstrated that heat transfer rate along the target plate was enhanced by an unsteady impinging jet. As the Reynolds number exceeding certain critical level, a steady to unsteady flow pattern transition for a confined laminar impinging jet with $\mathrm{Re}_j<1000$ was numerically investigated by Chiriac and Ortega [18]. They also indicated that the critical jet Reynolds number for the onset of unsteady flow was between 585 and 610. Moreover, the dominant frequency of the unsteady jet flow is in accordance with the primary vortices emanating from the shear layer produced by the jet just issued from the nozzle. The transition between the laminar and turbulent impinging jet flow at Re_j=1,500 was suggested by Elison and Webb [19]. A combined experimental and numerical study was carried out by Narayanan et al. [20] to study an impinging slot jet flow. They noted that the secondary peak in the heat transfer coefficient was still high owing to the interaction between the streamwise velocity variance and related motion in the outer region and to the near-wall turbulence.

Colucci and Viskanta [21] examined the effects of the nozzle geometry on the impinging jet heat transfer. They compared the results measured with two different hyperbolic nozzles and pointed out that the outer peak of the local heat transfer coefficient was dependent upon the geometry of the nozzle. Ashforth-Frost and Jambunathan [22] suggested that the length of potential core in an impinging jet could be affected by the jet confinement and the potential core was longer for a fully developed jet exit velocity profile than a flat jet exit velocity profile. Baydar [23] experimentally investigated confined impinging jets at low Reynolds number and showed that a low pressure zone appeared on the impinging plate for both single and double jets as the nondimensional nozzle-to-plate spacing (H/D) was less than 2. Furthermore, heat transfer in multiple jets impinging onto a plate was investigated by San and Lai [24]. They obtained an optimum ratio of the jet-to-jet spacing to jet diameter and proposed a correlation for stagnation Nusselt number. Recently, in our research group Hsieh et al. [25] visualized the detailed flow patterns of a round air jet impinging onto a heated disk confined in a cylindrical chamber and revealed that inclining the chamber top could effectively suppress the buoyancy-induced vortex flow.

In the impinging jet flow encountered in the CVD and RTP processes, the gas jet is at a relatively low flow rate and the buoyancy in the flow is no longer small compared with the jet inertia. Significant flow recirculation can be induced by the buoyancy and the impinging jet flow is driven by the combined effects of the inertia and buoyancy. The importance of the buoyancy on the recirculation flow in a vertical CVD reactor was illustrated by Wahl [26]. Similar investigations have been carried out for various types of CVD reactors including the metal organic CVD reactors [27-30] and single RTP processors [31-33]. In these studies for semi-conductor thin film deposition [31-33] various vortex flow patterns were reported in the impinging jet flow.

1.3 Objective and Scope of Present Study

The above literature review clearly reveals that various aspects of the flow and heat transfer associated with the inertia dominated high speed impinging jets have been extensively investigated. However, the complex flow structures and the associated thermal characteristics for the impinging jets simultaneously driven by the jet inertia and buoyancy remain poorly understood. In an initial attempt to investigate this mixed convective vortex flow, we [10] recently carried out an experimental study to delineate the steady and time periodic vortex flow patterns resulting from a vertically downward air jet impinging onto a horizontal heated disk confined in a vertical cylindrical chamber. For the ranges of parameters covered there for Q_j and ΔT respectively varied from 0 to 5.0 slpm (standard liter minute) and 0 to 25.0℃ at the jet-to-disk separation distance H=20.0 mm, the vortex flow was found to be mainly composed of two inertia-driven circular rolls and a buoyancy-driven circular rolls. At a high buoyancy-to-inertia ratio new rolls are generated and the flow becomes time-dependent. Over a certain range of the buoyancy-to-inertia ratio, a cyclic process characterized by the generation, growth, decay and disappearance of the new rolls prevails and the flow is time periodic. In this continuing study we re-conduct the experiment of Hsieh et al. [10] for H ranging from 10.0 to 30.0 mm over a wider range of the jet flow rate, intending to explore the possible presence of different vortex patterns, new forms of time-dependent vortex flow, and reverse flow transition at increasing buoyancy. Attention will be focused on the conditions leading to these special vortex flow structures and on the characteristics of these structures.

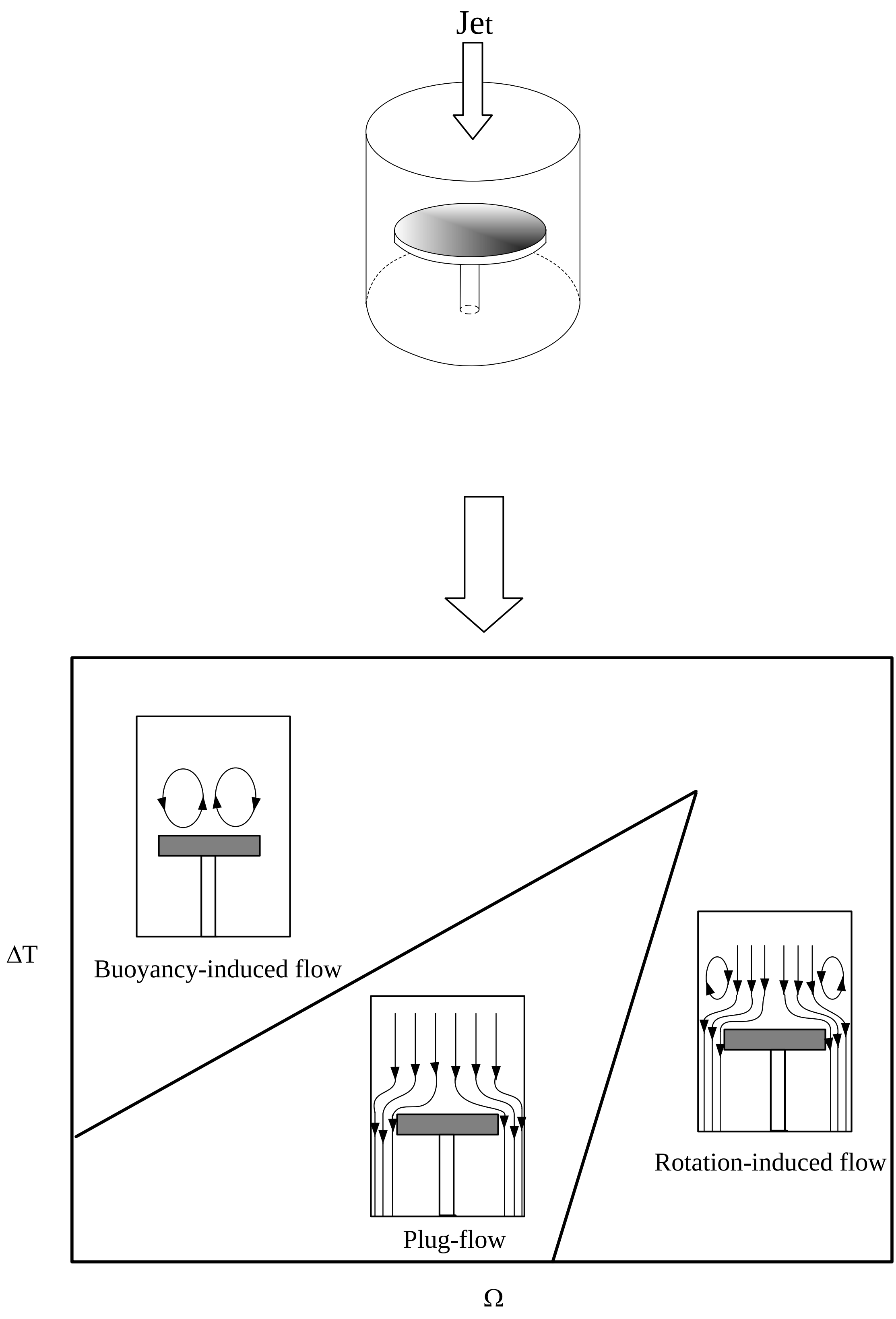

Fig. 1.1 Schematic of the flow patterns in a confined impinging jet depicting the plug-flow, buoyancy-induced flow and rotation-induced flow.

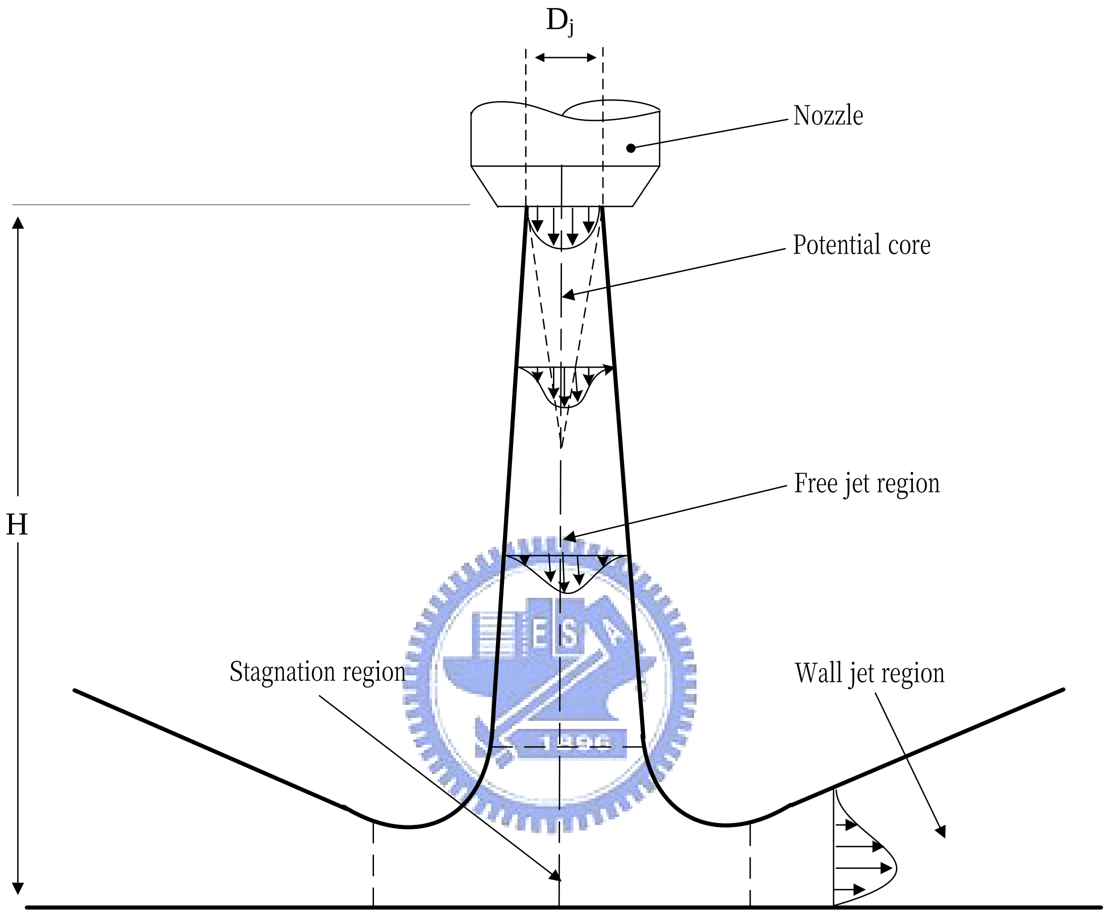

Fig. 1.2 Flow regimes associated with a circular jet impinging onto a flat plate.